Absolute photoionization cross sections along the Xe isonuclear sequence: Xe^{3+} to Xe^{6+}

J. M. Bizau,[1] C. Blancard,[2] D. Cubaynes,[1] F. Folkmann,[3] J. P. Champeaux,[2] J. L. Lemaire,[3] and F. J. Wuilleumier[1]
[1]*Laboratoire d'Interaction des Rayons X avec la Matière (LIXAM), UMR 8624 du CNRS, Université Paris-Sud, B. 350, and Laboratoire pour l'Utilisation du Rayonnement Electromagnétique (LURE), 91405-Orsay cedex, France*
[2]*CEA DAM Ile-de-France, DPTA, Boîte Postale 12, F-91680 Bruyères-le-Châtel, France*
[3]*Department of Physics and Astronomy, University of Aarhus, DK-8000 Aarhus C, Denmark*
(Received 28 October 2005; published 24 February 2006)

Absolute photoionization cross sections of Xe^{3+} to Xe^{6+} ions have been measured over an extended photon energy range from the first ionization threshold to 160 eV. Single and double photoionization cross sections have been obtained. In the case of Xe^{3+} and Xe^{6+} ions, two completely independent setups, both based on the merged beam technique, have been used. Multiconfiguration Dirac-Fock calculations were performed to interpret the spectra in the region of $4d$ electron excitations. The partition of the oscillator strength between the discrete photoexcitation and the direct photoionization channels in the $4d$ subshell has allowed us to follow precisely the collapse of the $4f$ wave function for these ions of the isonuclear series of Xe.

DOI: 10.1103/PhysRevA.73.022718 PACS number(s): 32.80.Fb, 32.80.Hd

I. INTRODUCTION

One of the very first experiments using synchrotron radiation, the measurement of the photoabsorption cross section of neutral Xe by Ederer [1] in the photon energy range involving the excitation of a $4d$ electron, brought a rather surprising result. Instead of a strong $4d \rightarrow 4f$ transition which would be expected to be observed below the $4d$ thresholds, it revealed the existence of a broad and intense structure above the threshold, while discrete excitation lines were completely absent. These observations were first explained within the frame of the one-electron model [2], although the absolute value of the cross section and the energy position of the maximum of the cross section could be reproduced theoretically only later by taking into account the full correlation and polarization effects [3]. The qualitative explanation resides in the existence of a double well produced by a strong centrifugal repulsion for $l=3$ in the effective f potential $V_{eff}=-Z/r+l(l+1)/2r^2$. In neutral Xe, the major part of the nf wave functions lies in the outer well. Therefore the overlap with the bounded $4d$ orbital is very weak, explaining the absence of the discrete $4d \rightarrow nf$ transitions. On the opposite, the wave function of energetic continuum electrons (with kinetic energy ε of the order of the height of the centrifugal barrier) can penetrate the core and is responsible for the broad $4d \rightarrow \varepsilon f$ structure in the continuum.

Another key study for the understanding of the behavior of the $4f$ wave function in the $Z=51-58$ elements was the resonant laser-driven experiment of Lucatorto *et al.* [4]. Their first measurements of the $4d$ photoabsorption spectra of Ba, Ba^+, and Ba^{2+} revealed that, while the spectra of Ba and Ba^+ are quite similar and show (in a way comparable to Xe) a broad structure above the $4d$ thresholds and weak discrete lines below, the spectrum of Ba^{2+} is completely different. Four strong discrete lines were observed, and the maximum value reached by the cross section in the continuum was only 60% of the value for Ba^+. These observations on Ba^{2+} compared to neutral Ba were qualitatively interpreted by a collapse of the $4f$ wave function into the inner well as the electron screening of the nuclear attraction is lowered by the removal of the two outer electrons. Then a transfer of the $4d$ oscillator strength occurs from the continuum part of the cross section to the discrete part. An intense discussion followed for the assignment of the discrete lines (for a detailed review on the studies related to the contraction of the $4f$ wave function, see Kjeldsen *et al.* [5] and references therein). A convincing interpretation was given by Clark [6] on the basis of multiconfiguration Dirac-Fock (MCDF) calculations.

In a previous experiment, we measured the relative photoionization cross sections for ions of the isonuclear sequence of Xe: Xe^{4+} to Xe^{7+} [7]. This experiment, using the merged beam technique implemented by Lyon and co-workers [8], combined the use of an electron cyclotron resonance ion source (ECRIS) for the production of multiply charged ions with synchrotron radiation. The interpretation of the data was based on MCDF calculations. This study was an extension of the work of Koizumi *et al.* [9] on Xe^+ to Xe^{3+} accomplished at the Photon Factory using an electron-impact-type ion source; see also Sano *et al.* [10]. We concluded that the contraction of the nf orbitals was gradually increasing from the Xe^+ ion, which has a spectrum quite similar to neutral Xe, to be complete only for Xe^{5+} which exhibits a regular $4d \rightarrow nf$ Rydberg series without measurable continuum cross section. In our former work [7], only relative photoionization cross sections were reported because the efficiency of the ion detector was not measured.

Experimental photoionization studies on the contraction of the $4f$ orbital in ions of elements in the range $Z=51-58$ have been extended to isonuclear series of Xe (Xe^{6+} to Xe^{8+} [11], Sb (Sb^+ to Sb^{3+} [12]), and I (I, I^+, I^{2+} [13], Sb^{9+} to Sb^{14+} [14]), as well as to isoelectronic series of Xe (Ba^{2+}, La^{3+} [15]) using dual laser produced plasmas photoabsorption technique. Nevertheless, such a technique is not able to determine absolute cross sections. In opposite, the merged beam experiments presently in operation at ASTRID, the Photon Factory, Super ACO, and at the Advanced Light Source (ALS) have provided absolute cross sections for ions of the isonuclear series of I (I^+,I^{2+} [16]), Xe (Xe^+ [17]; Xe^+

and Xe^{2+} [18]; Xe^{3+} [19]), Ba (Ba^{2+} to Ba^{6+} [20], absolute cross sections up to Ba^{3+}; Ba^{+} and Ba^{2+} [5]) and of the isoelectronic series of Xe (I^{-}, Cs^{+}, Ba^{2+} [5]).

The aim of the present paper is to provide for Xe^{3+} to Xe^{6+} ions absolute photoionization cross sections both for single and double ionization and oscillator strengths. The energy region is extending from the first ionization threshold to 160 eV, including the region of $4d$ electron excitations. In such a way, trends in the distribution of the $4d$ oscillator strength between the discrete and continuum parts of the cross sections can be followed along the isonuclear series of Xe, from half filled up to totally bare $5p$ outer subshell. Compared to our previous paper [7], new MCDF calculations have been performed to interpret the $4d$ excitations spectra.

II. EXPERIMENT

The experiments were performed on the SU6 undulator beam line of the Super ACO positron storage ring in Orsay (LURE) and on the Miyake undulator beam line of ASTRID in Aarhus (ISA). The absolute photoionization cross sections were mainly measured in Orsay. In order to check the validity of these measurements, we measured also at ASTRID the absolute cross sections for Xe^{3+} and Xe^{6+}.

In the Orsay setup, as compared to the one previously used [7,20,21] and described in detail in Ref. [22], several improvements have been performed, in preparation for a new experiment which will be installed on the new storage ring SOLEIL presently under construction:

(i) A different ion source has been used. It is a permanent magnet 14-GHz ECRIS especially designed for this experiment at the CEA Grenoble. It has been optimized for the production of high currents of low to medium ($1 \leqslant q \leqslant 10$) charge ions. A rf power of 10 W was necessary for an optimum production of Xe^{3+} ions, and 100 W for Xe^{6+}.

(ii) The Wien filter, which was previously used for the selection in charge and mass of the ions at the exit of the ECRIS has been replaced by a 90° dipole magnet with high acceptance, allowing a better transmission and resolution in the selection of the species.

All other elements remain unchanged. In brief, after extraction from the ECRIS by a 6-kV extraction voltage and selection by the dipole magnet, the ion beam is decelerated by 2 kV to kinetic energy of $4 \times q$ keV before being merged with the monochromatized photon beam. After passing through a 2-mm hole collimator, a 20-cm-long interaction zone can be defined by application of a bias in the zone (typically −700 V). The overlap of the two beams in the interaction zone is optimized and measured by three sets of beam profilers situated at the beginning, the center, and the end of the region. Each set is composed of scanning wires in the horizontal and vertical planes. For these experiments, the ionic currents available in the interaction region were between 50 and 80 nA. After interaction with the photons, the ion beam is charge analyzed by two electrostatic deflectors placed in series. The parent beam current is measured in a Faraday cup. The ions which have increased their charge by one (or several) unit in the interaction (the so-called photoions) are counted using a multichannel plate detector.

In a first step, the photoionization cross sections are obtained by scanning the photon energy with no bias applied on the interaction region, and recording simultaneously the photoion counting rate, the parent ions current and the relative flux of photons on a gold mesh. This procedure allows the determination of relative cross sections only, but with good statistics due to the increase of the effective interaction length. The photon energy variation of the efficiency of the gold mesh is determined using an IRD AXUV 100TS Si photodiode calibrated in the PTB calibration facility in BESSY. A chopper placed on the photon beam line allows us to immediately subtract from the photoion signal the noise produced by charge stripping or collisional ionization by the residual gas in the interaction chamber. Several independent photon scans are added to determine the relative cross sections. They are later put on an absolute scale by the measurements, at some given photon energies, of all parameters needed for the determination of the absolute cross sections, i.e., the form factor (measuring the overlap between the two beams with bias applied on the interaction region) and the efficiency of the ion detector, in addition to the ones recorded during the photon scans. The relative accuracy on the cross sections was estimated to lie between 15 and 20 % [21]. The validity of our procedure for the determination of the absolute cross sections was checked by comparison of the measured cross section of He^{+} with the analytically calculated one, which is obtained with high precision in the case of a hydrogenlike ion [23]. The absolute photon energy is determined using resonant lines observed by photoabsorption in a noble gas cell, and is corrected for the Doppler shift.

In order to perform a cross check of our procedure, we have determined also at ASTRID the absolute cross sections for the Xe^{3+} and Xe^{6+} ions. The 10-GHz ECRIS which was used in our previous studies at Super ACO [22] was installed on the ASTRID experimental setup. The setup and the modifications performed for the installation of the ECRIS have been recently described in detail [24]. The Super ACO and ASTRID setups have many common characteristics. In particular, the performances of the photon beam lines are quite similar. Both are high flux (up to 10^{13} photons/sec/0.1% BP), and low resolution (typical resolving power of 1000) beam lines. The main differences of the setup at ASTRID compared to the one used in Orsay are the following ones:

(i) The collimator is situated before the merging of the two beams. This arrangement reduces the noise produced by charge stripping on the collimating slits.

(ii) There are five sets of scanning slits placed at regular intervals in a 50-cm-long interaction region. The complete automatization of the scanning procedure allows the direct determination of absolute photoionization cross sections during the photon energy scans.

(iii) A dipole magnet demerges the photoions from the parent ions.

(iv) The efficiency of the photodiode (Al_2O_3) is measured after each scan using a Samson double-collector noble gas ionization chamber [25].

(v) The implantation of the setup is permanent on the undulator beam line. This allows the use of larger ionic optics and, in principle, higher current available in the interac-

tion region. Nevertheless, the cross sections were recorded with less than 10 nA of Xe^{3+} and Xe^{6+}. This value is lower compared to the Super ACO experiment. It is probably due to the extraction optics that is not especially adapted to the ECRIS, but was designed for the Nielsen-type ion source which is known to have a much better emittance [24].

The great care taken in the design of the ASTRID experimental setup and in the determination of the various parameters during the photon scans allows the determination of the cross sections with an accuracy in the 10–15 % range, the best accuracy achieved up to now for such experiments.

III. THEORY

A multiconfiguration Dirac-Fock (MCDF) code [26], accounting for the Breit interaction and for radiative and finite nuclear mass corrections, has been used to analyze the observed spectra in the region of $4d$ excitations. In a first step, the wave functions and the energies are calculated. Then photoexcitation cross sections, radiative and Auger rates can be derived. These calculations require the knowledge of the initial and final states of the involved transitions. To achieve this goal, the one-electron orbitals are computed using a combination of the extended average level (EAL) method [27] and the Slater's transition state giving equal weight to the two involved states [28].

For the calculation of lines arising from the $4d$ subshell, the ground-state configuration is assumed to be $4d^{10}5s^25p^m$ with $m=3$ for Xe^{3+}, $m=2$ for Xe^{4+}, $m=1$ for Xe^{5+}, and $m=0$ for Xe^{6+}. The excited states are constructed from the $4d^95s^25p^mnp$ and $4d^95s^25p^mn'f$ configurations, with $n=5-9$ and $n'=4-9$, representing 3023 levels for Xe^{3+}, 2343 levels for Xe^{4+}, 968 levels for Xe^{5+}, and 181 levels for Xe^{6+}. The oscillator strengths are obtained both using length (L) and velocity (V) forms of the electric dipole matrix element for all the charge states. The theoretical spectra are obtained assuming a Lorentz profile for each line shape with a full width at half maximum (FWHM) of 20 meV. Then, for comparison with the experimental spectrum for a given charge state, the calculated spectra of the different initial levels are summed assuming a statistical population. The resulting spectrum is then convoluted with a Gaussian function to account for the finite experimental resolution. In the following, the oscillator strengths given in all tables are obtained from the area of the line in these spectra, using the formula [29]

$$f = 9.11 \times 10^{-3} \int_{h\nu_1}^{h\nu_2} \sigma(h\nu) dh\nu.$$

IV. RESULTS AND DISCUSSION

In the following, the results are presented in order of increasing charge state. Then the distribution of the oscillator strength between the resonant $4d \rightarrow mf, np$ and the continuum $4d \rightarrow \varepsilon f, \varepsilon p$ parts of the $4d$ photoionization cross section will be discussed along the Xe isonuclear series, revealing the degree of collapse of the $4f$ wave function as a function of the charge state.

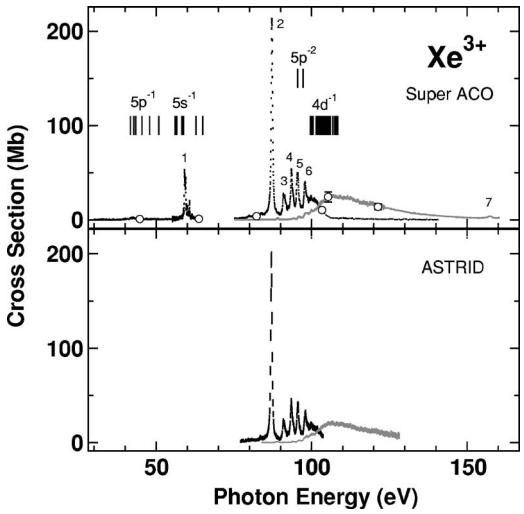

FIG. 1. Variation of the photoionization cross sections of the Xe^{3+} ion as a function of the photon energy. Upper panel: measurements at Super ACO; lower panel: measurements at ASTRID. The curves in black dots with error bars correspond to the cross section for the single ionization process $Xe^{3+}+h\nu \rightarrow Xe^{4+}+e^-$ as measured by the detection of the Xe^{4+} ions. The gray curve corresponds to the double ionization process $Xe^{3+}+h\nu \rightarrow Xe^{5+}+2e^-$ (resulting from the detection of the Xe^{5+} ion yield). The error bars on each dot represent the statistical uncertainty only. For the Super ACO data, the absolute measurements are shown as the open points with error bars giving the total uncertainty on the measured cross sections. The cross sections are obtained at ASTRID directly in absolute values (lower panel). The numbers above the resonant structures refer to Table I. The ionization thresholds for the Xe^{3+} ions in the ground level, obtained from our MCDF calculations, are shown as the vertical bars in the upper panel.

A. Xe^{3+} ion

The photoionization cross sections of the Xe^{3+} ion have been measured at Super ACO between 30 and 160 eV photon energy. They are shown in the upper panel of Fig. 1. The curve in black dots with error bars corresponds to the cross section for the single ionization process $Xe^{3+}+h\nu \rightarrow Xe^{4+}+e^-$, the gray curve corresponds to the photoionization cross section for the double ionization process $Xe^{3+}+h\nu \rightarrow Xe^{5+}+2e^-$. For all figures in the paper, the error bar on each dot represents the statistical uncertainty only. These curves are resulting from the photon energy scans obtained when the Xe^{4+} and Xe^{5+} ions are detected, respectively, giving relative cross sections only. They are placed on an absolute scale by normalization to the absolute measurements performed at some photon energies, shown as the open points in the figures. The error bars on these points give the total uncertainty on the measured cross sections.

The ground level of Xe^{3+} is $[Kr]\,4d^{10}5s^25p^3\,{}^4S_{3/2}$. The energy range covered here allows for ionization in the $5p$, $5s$, and $4d$ subshells. The energy of the thresholds of these processes, obtained from our MCDF calculations for the ions in the ground level, are indicated in the upper panel of Fig. 1 by the vertical lines, and labeled $5p^{-1}$ (final state of the photoionization process $Xe^{4+}\,[Kr]\,4d^{10}5s^25p^2+e^-$), $5s^{-1}$ (final state $Xe^{4+}\,[Kr]\,4d^{10}5s^15p^3+e^-$), and $4d^{-1}$ (final state

TABLE I. Energies in eV (column 2) and integrated oscillator strengths (measured at Super ACO, column 4, at ASTRID, column 5, and at ALS, column 6 [19]) of the resonant structures measured for the Xe^{3+} ion. The numbers in parentheses give the uncertainty on the last figure. Because each structure is composed of an extremely high number of unresolved lines, only the energy of the center of the structure is given. These data are compared with the results of our MCDF calculations (energies in column 3; oscillator strengths calculated in the *L* and *V* form assuming a statistical population of the levels in the ion beam in columns 7 and 8, respectively).

			Oscillator strength					
	Energy (eV)		Experiments			MCDF		
Line	Expt.	MCDF	SACO	ASTRID	ALS	*L*	*V*	Assignment
1	59.3	58.4	0.43 (12)		0.80 (20)	0.423	0.446	$4d \rightarrow 5p$
2	87.1	87.5	1.55 (28)	1.47 (22)		1.056	0.744	$4d \rightarrow 4f$
3	91.0	90.5	0.36 (6)	0.28 (4)		0.311	0.218	
4	93.5	93.1	0.50 (9)	0.42 (6)		0.405	0.284	
5	95.5	94.8	0.49 (9)	0.40 (6)		0.448	0.307	
6	97.9	97.2	0.52 (9)	0.40 (6)		0.323	0.220	
7	157.3		0.027 (5)					$4p \rightarrow 5d$

Xe^{4+} [Kr] $4d^9 5s^2 5p^3 + e^-$), respectively. Resonant structures, labeled 1–7, are clearly observed in the spectra of Fig. 1. The energy of the center of the structures and their integrated oscillator strength are listed in columns 2 and 4 of Table I.

The cross sections measured at ASTRID between 80 and 130 eV photon energy are shown in the lower panel of Fig. 1. These measurements have been performed with an excitation band pass of the order of 300 meV at 90 eV, compared to 100 meV for the Super ACO experiment. The oscillator strength of the resonant structures is given in column 5 of Table I. Considering the oscillator strengths and the double ionization spectra, which are independent on the excitation band pass, the two independent measurements of Super ACO and ASTRID are in very good agreement within their respective uncertainty, giving confidence into the validity of our determination of the cross sections. The measurements by Emmons *et al.* [19] performed at the ALS for Xe^{3+} with a higher resolution, are in overall agreement with our results. In their work, however, the absolute cross sections have been determined in the energy range 57–115 eV only, with a moderate accuracy of 25%. In the present work, we have been able to determine the cross sections in absolute values over the whole photon energy range 35–160 eV, and with an improved accuracy.

In the following, we discuss the different regions of the spectra in order of increasing photon energy.

1. Region of the first ionization thresholds ($5p^{-1}$)

A magnification of the 35–50-eV region, including the ionization thresholds in the $5p$ subshell ($5p^{-1}$), is shown in Fig. 2. This spectrum was recorded using an Al filter in order to reject the contribution of higher-order radiations diffracted by the monochromator. The curve represents the photoionization cross section of the $5p$ subshell of Xe^{3+} ion. Its value is 0.80 ± 0.16 Mb at 44.7 eV close to threshold, i.e., it is of the same order as the $5p$ cross section in neutral Xe in the similar energy range (1.1 ± 0.2 Mb) [30].

Of particular interest for studying this region is the investigation of the possible contamination of the ion beam by metastable states produced in the ECRIS. All levels with the same configuration as the ground level (multiplets Xe^{3+} [Kr] $4d^{10}5s^2 5p^3$ $^2D_{3/2}$, $^2D_{5/2}$, $^2P_{1/2}$, $^2P_{3/2}$) are metastable due to the parity selection rule, with life times longer than the time of flight spent by the Xe^{3+} ions to arrive into the interaction zone, typically a few microseconds. Then the Xe^{3+} ions in the ground level and in the metastable levels will interact with the photons. The relative population of the ions in the different levels can be estimated from the appearance of several ionization thresholds in the experimental spectrum [21]. Each populated metastable level will produce a step in the photoionization cross section at a photon energy lower than the step due to the ions in the ground level by a quantity equal to the excitation energy of the metastable level. The excitation energies of the $^2D_{3/2}$, $^2D_{5/2}$, $^2P_{1/2}$, $^2P_{3/2}$ levels have been deduced by Reyna Almandos *et al.* [31], from their measurements, to be 1.645, 2.171, 3.476, and 4.420 eV, respectively. Our calculated values are 0.6 eV

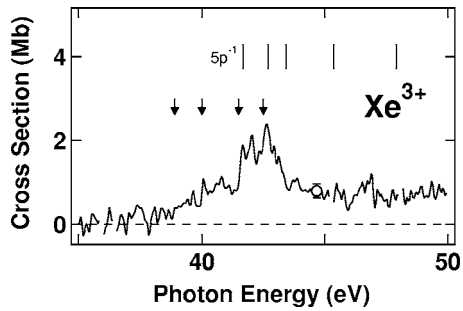

FIG. 2. Variation of the photoionization cross section of the Xe^{3+} ion in the 35–50-eV photon energy range. The excitation band pass was of the order of 150 meV. The vertical lines above the spectrum indicate the $5p^{-1}$ ionization thresholds (configuration Xe^{4+} [Kr] $4d^{10}5s^2 5p^2$) obtained from our MCDF calculations for the Xe^{3+} ions in the ground level. The vertical arrows indicate the position of the thresholds as assigned in Table II.

TABLE II. Energies and assignments of Xe^{3+} ionization thresholds. The thresholds around 40 and 90 eV correspond to the processes Xe^{3+} [Kr] $4d^{10}5s^25p^3\ ^{2S+1}L_J+h\nu \rightarrow Xe^{4+}$ [Kr] $4d^{10}5s^25p^2\ ^3P_{0,1}+e^-$, and [Kr] $4d^{10}5s^25p^3\ ^4S_{3/2}+h\nu \rightarrow Xe^{5+}$ [Kr] $4d^{10}5s^25p\ ^2P_{1/2,3/2}+e^-$, respectively. The accuracy on the experimental energies is estimated to be ±0.2 eV.

Energy (eV)		
Expt.	MCDF	Assignment
	37.39	$Xe^{3+}\ ^2P_{1/2} \rightarrow Xe^{4+}\ ^3P_0$
38.9	38.98	$Xe^{3+}\ ^2D_{5/2} \rightarrow Xe^{4+}\ ^3P_0$
40.0	40.03	$Xe^{3+}\ ^2D_{3/2} \rightarrow Xe^{4+}\ ^3P_0$
41.5	41.67	$Xe^{3+}\ ^4S_{3/2} \rightarrow Xe^{4+}\ ^3P_0$
42.5	42.70	$Xe^{3+}\ ^4S_{3/2} \rightarrow Xe^{4+}\ ^3P_1$
93.7	95.43	$Xe^{3+}\ ^4S_{3/2} \rightarrow Xe^{5+}\ ^2P_{1/2}$
95.5	97.33	$Xe^{3+}\ ^4S_{3/2} \rightarrow Xe^{5+}\ ^2P_{3/2}$

higher, at 2.206, 2.716, 4.322, and 5.144 eV, respectively. In Fig. 2, the signal becomes statistically significant around 38.9 eV, and increases gradually with some steps around 40, 41.5, and 42.5 eV photon energy, shown as vertical arrows in Fig. 2. Although they were carried out with a different ECRIS, our observations are consistent with the relative cross section measured by Emmons *et al.* [19], who observed the appearance of the signal at 37.8 eV, as well as a clear step at 42.39 eV. They interpreted these two features as the thresholds for Xe^{3+} ions in the $^2P_{3/2}$ and $^4S_{3/2}$ levels, respectively, although the $^4S_{3/2}$ threshold had to be shifted down to 42.2±0.2 eV to be compatible with the excitation energy of the $^2P_{3/2}$ level given in Ref. [31]. In Table II, we propose an alternative interpretation, based on our MCDF calculations and taking into account the splitting of the Xe^{4+} [Kr] $4d^{10}5s^25p^2$ configuration into the $^3P_0$, $^3P_1$, $^3P_2$, $^1D_2$, and $^1S_0$ levels. For these levels we determined the ionization threshold of the Xe^{3+} ions in the ground level to be at 41.67, 42.70, 43.43, 45.41, and 47.96 eV, respectively. Their position is shown as the vertical bars in Fig. 2 (labeled $5p^{-1}$). Then the step at 41.5±0.2 eV can be interpreted as corresponding to the threshold for the photoionization process Xe^{3+} [Kr] $4d^{10}5s^25p^3\ ^4S_{3/2}+h\nu \rightarrow Xe^{4+}$ [Kr] $4d^{10}5s^25p^2\ ^3P_0 + e^-$. The proposed assignment of the other thresholds is summarized in Table II.

In conclusion, it appears that most of the levels in the Xe^{3+} [Kr] $4d^{10}5s^25p^3$ configuration are populated in our ion beam. The assignment we propose here is tentative only. Many resonant structures, clearly visible in Fig. 2 and in the spectrum of Emmons *et al.* [19], are superimposed on the direct continuum cross section. They make it difficult to determine the exact position of the thresholds and the relative height of each step. For these reasons, we have assumed a statistical population of the levels in the following. This is justified considering the low excitation energy of the levels compared to the "electronic temperature" of the ECRIS plasmas.

2. Region of the $4d \rightarrow mf,np$ excitations

The photoionization cross sections measured at Super ACO in the region of the $4d \rightarrow 5p$ (structure 1 in Fig. 1) and

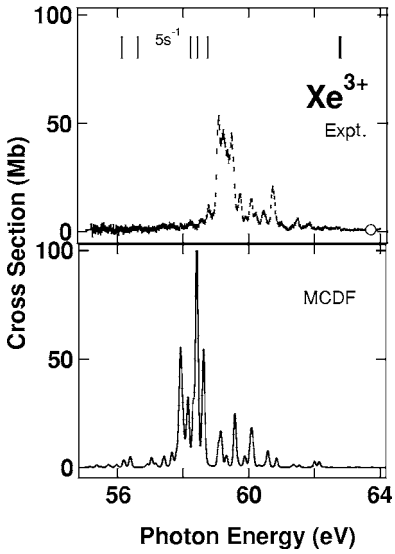

FIG. 3. Variation of the photoionization cross section of the Xe^{3+} ion in the region of the $4d \rightarrow 5p$ excitations. Upper panel: Super ACO results. The excitation band pass was of the order of 75 meV. The open point gives the absolute determination of the cross section. Lower panel: results of our MCDF calculations (L form) obtained assuming a statistical population of the ions in the ground and metastable levels. The vertical lines above the experimental spectrum indicate the $5s^{-1}$ ionization thresholds (configuration Xe^{4+} [Kr] $4d^{10}5s^15p^3$) as obtained from the MCDF calculations for the Xe^{3+} ions in the ground level.

$4d \rightarrow mf,np$ $(m>3, n>5)$ transitions are presented in the upper panel of Figs. 3 and 4, respectively. They are compared with the results of the MCDF calculations (L form) shown on the lower panels. The calculations reproduce qualitatively well the resonant structures of the spectra, which correspond to processes of the type

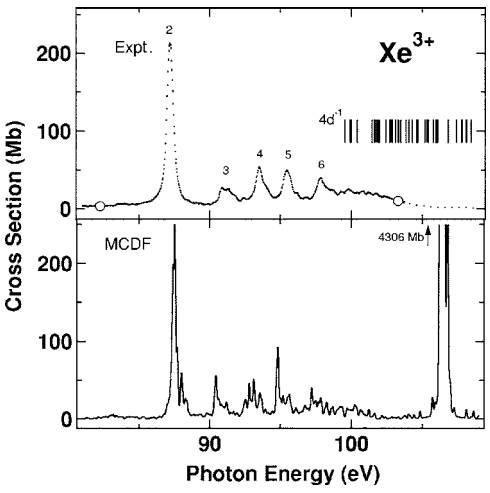

FIG. 4. Variation of the photoionization cross section of the Xe^{3+} ion in the region of the $4d \rightarrow np,mf$ $(n>5, m>3)$ excitations. The only differences with Fig. 3 are the experimental band pass of 100 meV and the vertical bars giving here the position of the calculated $4d^{-1}$ ionization thresholds (configuration Xe^{4+} [Kr] $4d^95s^25p^3$).

$$\mathrm{Xe}^{3+}\,[\mathrm{Kr}]\,4d^{10}5s^25p^3 + h\nu$$
$$\rightarrow \mathrm{Xe}^{3+}\,[\mathrm{Kr}]\,4d^9 5s^2 5p^3 np,mf$$
$$(n>4, m>3)\ \text{(photoexcitation)}$$
$$\hookrightarrow \mathrm{Xe}^{4+} + e^-\ \text{(autoionization)}.$$

In particular, the grouping of the resonances into five equally spaced main structures observed in Fig. 4 is well described. Quantitatively, only the oscillator strength for the $4d \rightarrow 5p$ transition is correctly calculated both in the L and V form, but with too low an energy by 1 eV (see Table I). All other ones are underestimated, the L form giving the best agreement with experiment. The MCDF calculations predict a piling of the oscillator strength at high photon energy leading to a large structure at 106.5 eV. This structure, which we called "broom resonance" in the following, is not observed in the experimental spectrum. It appears to result from an artifact in the calculations. The oscillator strength which is ascribed to transitions to the highest Rydberg states included in the calculations has frequently been observed to be anomalously large. This has previously been commented by Raasen *et al.* [32], and is related to the truncation of the basis set used in the calculation [33–35]. We will see in the following that this anomalous intensity of the transitions to the highest Rydberg states included in the calculations appears in most of the Xe ion charge states. We will go back to the discussion of this point at the end of the paper. Its existence could explain the underestimation of the calculated oscillator strengths as compared to the measured ones. The calculations also indicate that each structure is composed of a large number of unresolved lines. One indication of the complexity of the spectrum is the number of $4d^{-1}$ ionization thresholds shown in Fig. 4 (labeled $4d^{-1}$). The Xe^{4+} $[\mathrm{Kr}]\,4d^9 5s^2 5p^3$ configuration supports 36 levels, ranging from 99.54 to 108.47 eV according to the MCDF calculations. Each threshold is the limit of one or several Rydberg series. The situation is even more complicated when one considers the population of the metastable levels in the ion beam. Due to this complexity, we did not attempt to assign the different structures in Table I. We can assume that the most intense line at 87.1 eV (structure 2) has a main $4d \rightarrow 4f$ character, with a strong perturbation by $4d \rightarrow 5f$ and $4d \rightarrow 6p$ components. Nevertheless, the behavior of the cross section is still very far from a regular $4d \rightarrow nf$ Rydberg series.

Our cross section is also in qualitative agreement with the measurements presented in Ref. [19], taking into account the difference in energy resolution. But we measure here a significantly lower oscillator strength for the $4d \rightarrow 5p$ excitations, even when taking into account the respective uncertainty of the two measurements (see Table I).

3. Double ionization

The variation of the double ionization cross section (processes $\mathrm{Xe}^{3+} + h\nu \rightarrow \mathrm{Xe}^{5+} + 2e^-$) measured at Super ACO between 75 and 160 eV is shown in Fig. 5. The energies of the double ionization thresholds (levels Xe^{5+} $[\mathrm{Kr}]\,4d^{10}5s^25p^2P_{1/2}$, $^2P_{3/2}$), labeled $5p^{-2}$ in Fig. 5, have been calculated for the Xe^{3+} ions in the ground level to be at 95.43 and 97.33 eV, respectively. They are just below

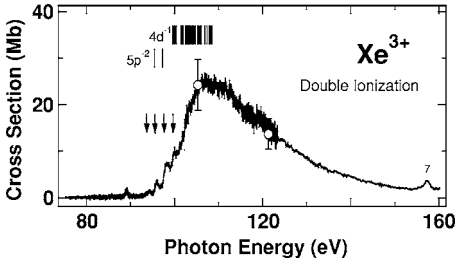

FIG. 5. Variation of the double ionization cross sections of the Xe^{3+} ion measured at Super ACO as a function of the photon energy. Same caption as Fig. 4. The calculated position of the double ionization thresholds is also shown as vertical bars (labeled $5p^{-2}$).

the $4d^{-1}$ ionization thresholds, extending above 99.54 eV. In the experimental cross section, a resonance in the signal appears at 89.01 eV. Then steps are observed around 93.7, 95.5, 97.6, and 99.6 eV, shown as vertical arrows in Fig. 5. They might be associated with the opening of the double ionization and $4d^{-1}$ thresholds. A tentative assignment for some of these steps is given in Table II. The observation of signal below 90.3 eV implies the existence of higher excited metastable states in the ion beam. The $5s^25p^2(^3P)5d\ ^4F$ term locates levels around 17 eV excitation energy [31]. This term is metastable in LS coupling only. Our data tend to indicate that LS coupling is still a good approximation for the description of this term in the Xe^{3+} ion. Then the line at 89.01 eV can probably be associated with a resonant Auger process of the type

$$\mathrm{Xe}^{3+}\,[\mathrm{Kr}]\,4d^{10}5s^25p^25d + h\nu$$
$$\rightarrow \mathrm{Xe}^{3+}\,[\mathrm{Kr}]\,4d^9 5s^2 5p^2 5dnp,mf$$
$$(n>5, m>3)\ \text{(photoexcitation)}$$
$$\hookrightarrow \mathrm{Xe}^{4+}\,[\mathrm{Kr}]\,4d^9 5s^2 5p^2 5d + e^-\ \text{(decay step 1)}$$
$$\hookrightarrow \mathrm{Xe}^{5+}\,[\mathrm{Kr}]\,4d^{10}5s^25p + e^-\ \text{(decay step 2)}.$$

The Xe^{4+} $[\mathrm{Kr}]\,4d^{10}5s5p^3$ configuration was proposed in Ref. [19] for decay step 1. This is not supported by our MCDF calculations placing the levels of the Xe^{4+} $[\mathrm{Kr}]\,4d^{10}5s5p^3$ configuration 30 eV below the Xe^{5+} $[\mathrm{Kr}]\,4d^{10}5s^25p$ ground level, thus forbidding decay step 2. Let us note that the line at 89.01 eV does not correspond to any intense structure in the single ionization cross section. Resonant Auger processes are also present at higher photon energies, and affect the determination of the position of the thresholds. Above the $4d^{-1}$ thresholds, we observe the direct Auger decay of the $4d$ hole, according to

$$\mathrm{Xe}^{3+}\,[\mathrm{Kr}]\,4d^{10}5s^25p^3 + h\nu$$
$$\rightarrow \mathrm{Xe}^{4+}\,[\mathrm{Kr}]\,4d^9 5s^2 5p^3 + e^-$$
$$\text{(direct photoionization in } 4d \text{ subshell)}$$
$$\hookrightarrow \mathrm{Xe}^{5+}\,[\mathrm{Kr}]\,4d^{10}5s^25p + e^-\ \text{(Auger decay)}.$$

This is likely to be the dominant process in the double ionization cross section. The maximum of the cross section is reached at 106.5 eV, below the last $4d^{-1}$ ionization threshold calculated to be at 108.47 eV. The value of the maximum is

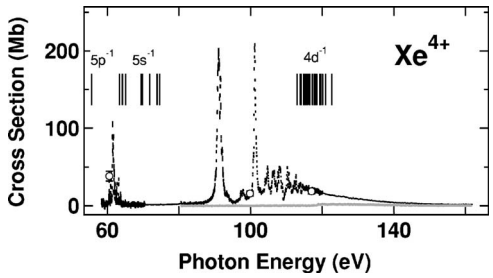

FIG. 6. Variation of the photoionization cross sections of the Xe^{4+} ion as a function of the photon energy. The curves in black dots with error bars correspond to the cross section for the single ionization process $Xe^{4+}+h\nu \rightarrow Xe^{5+}+e^-$ (detection of the Xe^{5+} ions), and the gray curve corresponds to the double ionization process $Xe^{4+}+h\nu \rightarrow Xe^{6+}+2e^-$ (detection of the Xe^{6+} ions). The error bars on each dot represent the statistical uncertainty. The absolute measurements are shown as the open points with error bars giving the total uncertainty on the measured cross sections. The ionization thresholds in the $5p$, $5s$, and $4d$ subshells of the Xe^{4+} ions initially in the ground level, obtained from our MCDF calculations, are shown as the vertical bars in the upper panel.

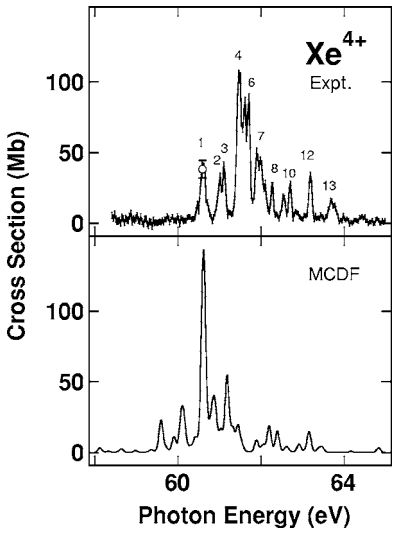

FIG. 7. Variation of the single photoionization cross section of the Xe^{4+} ion in the region of the $4d \rightarrow 5p$ excitations. Upper panel: Super ACO experiment. The excitation band pass was of the order of 75 meV. The open point gives the absolute determination of the cross section. The numbers above the resonant structures refer to Table III. Lower panel: results of our MCDF calculations (L form) obtained assuming a statistical population of the ions in the ground and metastable levels.

25±6 Mb in the Orsay measurements, and 20±3 Mb in the ASTRID one, in good agreement one with each other, giving an average value of 21±3 Mb. The value 30±7 Mb measured at the ALS is significantly higher [19], staying, however, within the respective uncertainties. Our value is lower than the cross sections published for neutral Xe (27.1 ±0.8 Mb [36]) and for Xe^+ and Xe^{2+} ions (27±3 Mb [18]), demonstrating that the $4f$ wave function begins to already collapse in Xe^{3+} ions.

A broad line (structure 7 in Figs. 1 and 5) is clearly seen at 157.3 eV. It is tentatively interpreted as due to $4p \rightarrow 5d$ transitions (see Table I). Nevertheless, our calculations predict these transitions to be at a significantly higher photon energy, around 169 eV, and the $4p^{-1}$ thresholds to lie between 203.36 and 223.14 eV.

B. Xe^{4+} ion

The variation of the single and double photoionization cross sections of Xe^{4+} ion is shown in Fig. 6 between 58 and 162 eV photon energy. The ground level of Xe^{4+} is $[Kr]\ 4d^{10}5s^25p^2\ ^3P_0$. All other levels with the same configuration are metastable and contribute to the observed signal together with the ground level. We have calculated the excitation energy of these levels to be 1.026, 1.755, 3.730, and 6.279 eV for the $^3P_1$, $^3P_2$, $^1D_2$, and $^1S_0$ levels, respectively. In the following, we have assumed a statistical population of the ions in these various levels. The energy range here examined is beginning just above the first ionization threshold, calculated to be at 53.749 eV, and corresponding to the Xe^{5+} $[Kr]\ 4d^{10}5s^25p^1\ ^2P_{1/2}$ level (the $^2P_{3/2}$ threshold is at 55.649 eV; it is labeled $5p^{-1}$ in Fig. 6). We did not observe any significant signal in this energy range, indicating that the $5p$ photoionization cross section is probably not more than 1 Mb at threshold. When compared to the Xe^{3+} cross section presented in Fig. 1, several spectacular differences are evident: the intensity of the double ionization cross section above the $4d^{-1}$ thresholds is strongly reduced, and is partly transferred to the single ionization channel; there is a strengthening of the $4d \rightarrow mf,np$ excitations, in particular with the appearance of a second strong line around 101 eV. These observations give evidence of a strongly increasing collapse of the $4f$ wave function.

1. $4d \rightarrow mf,np$ discrete transitions

The single photoionization cross section measured at Super ACO in the region of the $4d \rightarrow 5p$ and $4d \rightarrow mf,np$ $(m>3, n>5)$ transitions is presented in the upper panel of Figs. 7 and 8, respectively. It is compared to the results of the MCDF calculations in the L form, which is shown in the lower panels. Here too the calculations reproduce rather well the resonant structures of the spectra, which correspond to processes

$$\begin{aligned} &Xe^{4+}\,[Kr]\,4d^{10}5s^25p^2 + h\nu \\ &\quad \rightarrow Xe^{4+}\,[Kr]\,4d^9 5s^2 5p^2 np,mf \\ &\quad\quad (n>4, m>3)\ \text{(photoexcitation)} \\ &\quad\quad \hookrightarrow Xe^{5+} + e^-\ \text{(autoionization)}. \end{aligned}$$

The energy positions and the integrated oscillator strengths of the observed $4d \rightarrow 5p$ transitions are given in Table III. They have been obtained using a procedure fitting the spectrum by a sum of Gaussian profiles. They are compared with the results of the MCDF calculations obtained in the L and V form, assuming a statistical population of the Xe^{4+} ion in the ground and metastable levels. Compared to the same transitions in the Xe^{3+} ion shown in Fig. 3, there is only a small shift of 2 eV towards higher photon energies,

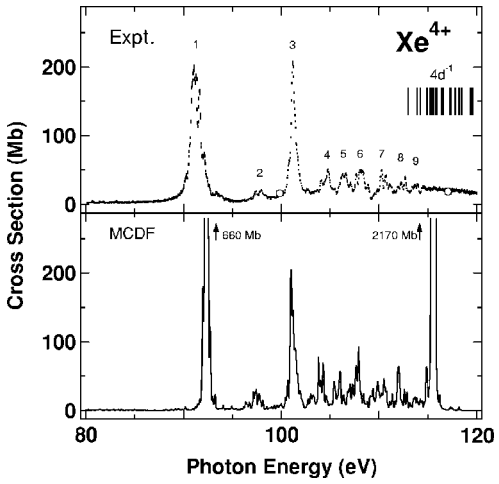

FIG. 8. Variation of the photoionization cross section of the Xe^{4+} ion in the region of the $4d \rightarrow np,mf$ $(n>5,m>3)$ excitations. The experimental band pass is equal to 100 meV here, and the numbers over the structures refer to Table IV. The vertical bars give the position of the calculated $4d^{-1}$ ionization thresholds (configuration Xe^{5+} [Kr] $4d^9 5s^2 5p^2$).

resulting from the decrease of the screening of the nuclear attraction by the outer $5p$ electrons when one of them is removed. We note also a significant increase in the oscillator strength for the sum of the transitions ($f=0.82\pm0.14$). As for the Xe^{3+} ion, the MCDF spectrum is shifted by 1 eV towards lower energy as compared to the experimental one, but it gives now a lower value for the sum of the oscillator strength of the transitions ($f=0.60$, which is the average of L- and V-form results).

TABLE IV. Energies and integrated oscillator strengths of the $4d \rightarrow mf,np$ transitions for the Xe^{4+} ion (the caption is the same as in Table III). Because of the extremely high number of unresolved lines in each structure, only the energy of the center of the structure is given.

	Energy (eV)		Oscillator strength Experiment	MCDF		
Line	Expt.	MCDF	SACO	L	V	Assignment
1	91.1	92.4	2.90 (59)	2.71	1.83	$4f,5f$
2	97.7	97.5	0.34 (7)	0.29	0.18	$5f(7p,6f)$
3	101.2	101.1	1.63 (32)	1.18	0.73	$6f(7p)$
4	104.5	104.1	0.64 (13)	0.46	0.25	$6f(7p)$
5	106.4	105.7	0.48 (10)	0.34	0.22	$7f(6f)$
6	108.0	107.9	0.55 (11)	0.61	0.39	$7f(8p)$
7	110.6	110.3	0.53 (11)	0.48	0.29	$8f,9f(7f)$
8	112.3	112.0	0.34 (7)	0.38	0.23	$9f$
9	113.7		0.25 (5)			

In the case of the $4d \rightarrow np,mf$ $(n>5,m>3)$ transitions, the MCDF calculations reproduce well the position and the integrated intensity of the nine main structures which are visible in Fig. 8, and labeled 1–9. The experimental and theoretical energy positions, as well as the integrated oscillator strengths of these structures, are given in Table IV. Because these structures are clearly composed of a large number of unresolved lines, we give in the table only the position of the center of the structures. The assignments given in the last column correspond to the nl final subshell of the $4d \rightarrow nl$ transitions having the highest calculated intensity, with the

TABLE III. Energies (column 2) and integrated oscillator strengths (column 4) of the $4d \rightarrow 5p$ transitions for the Xe^{4+} ion. The numbers in parentheses give the uncertainty on the last figure. The experimental data are compared to the results of our MCDF calculations (energies: column 3; oscillator strengths calculated in the L and V form assuming a statistical population of the levels in the ion beam: columns 5 and 6, respectively). A tentative assignment of the lines resulting from our MCDF calculations is shown in column 7.

	Energy (eV)		Oscillator strength Experiment	MCDF		
Line	Expt.	MCDF	SACO	L	V	Assignment
1	60.64 (2)	59.596	0.060 (10)	0.028	0.031	$^3P_0 \rightarrow {}^3D_1$
2	61.04 (3)	60.169, 60.309	0.034 (6)	0.060	0.066	$^3P_2 \rightarrow {}^3P_2, {}^3P_1$
3	61.15 (2)		0.026 (5)			
4	61.51 (2)	60.583, 60.620	0.138 (23)			$^1S_0 \rightarrow {}^1P_1, {}^3P_2 \rightarrow {}^3D_3,$
5	61.64 (2)	60.635	0.063 (11)	0.270	0.271	$^1D_2 \rightarrow {}^3F_3$
6	61.74 (2)		0.059 (10)			
7	61.99 (2)	61.194	0.113 (19)	0.066	0.064	$^1D_2 \rightarrow {}^3D_3$
8	62.30 (2)	61.449	0.020 (4)	0.042	0.046	$^1D_2 \rightarrow {}^3F_2$
9	62.58 (2)	62.202	0.018 (3)	0.022	0.022	$^1D_2 \rightarrow {}^3D_2$
10	62.73 (2)	62.399	0.019 (3)	0.016	0.018	$^3P_2 \rightarrow {}^3P_1$
11	62.89 (4)		0.008 (2)			
12	63.22 (2)	62.924	0.029 (5)	0.017	0.017	$^3P_0 \rightarrow {}^3D_1$
13	63.74 (2)		0.025 (5)			

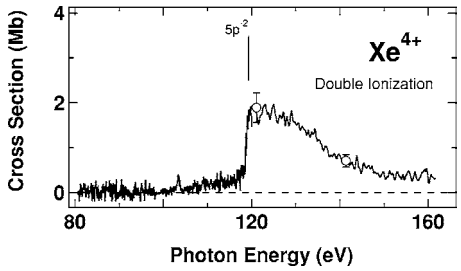

FIG. 9. Variation of the double ionization cross section of the Xe^{4+} ion as a function of the photon energy. The vertical line (labeled $5p^{-2}$) indicates the calculated position of the double ionization threshold (Xe^{6+} [Kr] $4d^{10}5s^2\ ^1S_0$ final level) for the Xe^{4+} ions in the ground level.

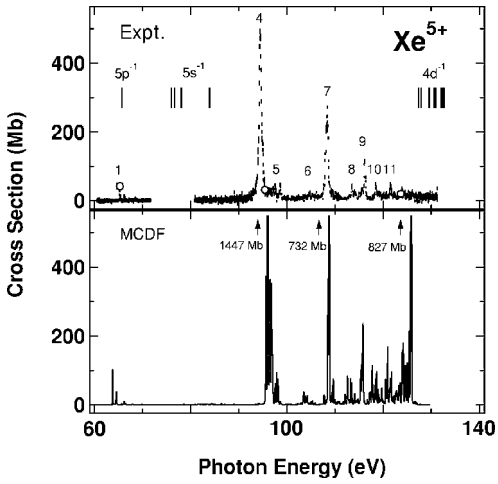

FIG. 10. Variation of the photoionization cross sections of the Xe^{5+} ion as a function of the photon energy. Upper panel: experiment. The curves in black dots with error bars correspond to the cross section for the single ionization process $Xe^{4+}+h\nu \rightarrow Xe^{5+}+e^-$ (detection of the Xe^{5+} ions). The error bars on each dot represent the statistical uncertainty. The absolute measurements are shown as the open points, with an error bar giving the total uncertainty on the measured cross section. Over the 100–120-eV energy range, the experimental band pass is of the order of 100 meV. Lower panel: results of our MCDF calculations (L form). The ionization thresholds for the Xe^{5+} ions in the ground level are shown as the vertical bars in the upper panel, as obtained from our MCDF calculations.

following smaller components in parentheses. The main difference between the experimental and theoretical spectra is in the energy position, higher by 1.3 eV in the MCDF spectrum, and in the intensity of structure 1. In opposite, the integrated oscillator strength is well reproduced by the L-form result. The V form gives systematically a lower value for all lines. Structure 1 brings by far the strongest contribution to all $4d \rightarrow 4f$ transitions, two-thirds of the intensity of the line according to the calculations when taking into account only the transitions with the highest oscillator strengths. The other one-third of the intensity is mainly composed of $4d \rightarrow 5f$ transitions. It is clearly broader in the experimental spectra than the other structures. The calculation of the autoionization rate for the Xe^{4+} [Kr] $4d^9 5s^2 4f 5p^2$ and Xe^{4+} [Kr] $4d^9 5s^2 5p^2 5f$ excited configurations indicates that they have a natural width of the order of 200 and 50 meV, respectively. We have calculated a radiative decay rate that is several orders of magnitude lower for these excited levels. Taking into account this broadening of structure 1 in the theoretical spectrum would bring the cross section value at the maximum of this structure to be in good agreement with the experimental one. Finally, we can also note a small contribution of $4d \rightarrow 6p$ transitions in this structure, which is visible in the experimental spectrum as the small bump on the high energy side, around 93.3 eV.

In Table IV, we have assigned the second structure in intensity (number 3) to $4d \rightarrow 6f$ transitions, according to the MCDF calculations. Let us note that a small contribution from $4d \rightarrow 7p$ transitions is also present. In a regular series, the $4d \rightarrow 5f$ transitions would be expected to be the strongest after the $4d \rightarrow 4f$ transitions. This is not the case here since we identified them as responsible for the smaller structure 2. This emphasizes the difficulty in assigning a transition between two configurations when the configuration interaction is very strong, as it is the case for the $4d \rightarrow nl$ transitions in the Xe^{4+} ion. The structures at higher energy have almost equal intensity, corresponding mainly to $4d \rightarrow nf$ transitions, with $n=7$, 8, and 9, each one spreading over an extended energy range. Finally, we note that the intensity of the broom resonance observed around 116 eV in the theoretical cross section is strongly decreased when compared to the Xe^{3+} ion, partly explaining the improvement in the agreement between the measured and calculated oscillator strengths.

2. $4d \rightarrow \varepsilon f, \varepsilon p$ continuum transitions

The variation, as a function of the photon energy, of the double ionization cross section measured for the Xe^{4+} ion is shown in the upper panel of Fig. 9. It is one order of magnitude lower than that of the Xe^{3+} ion (see Fig. 5). This results from two phenomena:

(i) Considering the increase of the oscillator strength for the $4d \rightarrow mf, np$ discrete transitions as compared to the Xe^{3+} ion, we expect the collapse of the $4f$ wave function to be effective for the Xe^{4+} ion. This must consequently result in a decrease of the $4d \rightarrow \varepsilon f, \varepsilon p$ continuum cross section.

(ii) The double ionization threshold, calculated at 119.32 eV for the Xe^{4+} ions in the ground level (labeled $5p^{-2}$ in Fig. 9), is located at the end of the energy range calculated for the $4d^{-1}$ thresholds extending from 112.97 to 122.69 eV. Only the Xe^{5+} $4d^{-1}$ levels above the double ionization threshold are able to decay to the Xe^{6+} ground level via Auger process, and contribute to the double ionization cross section according to

$$\begin{aligned} &Xe^{4+}\,[Kr]\,4d^{10}5s^2 5p^2 + h\nu \\ &\quad \rightarrow Xe^{5+}\,[Kr]\,4d^9 5s^2 5p^2 + e^- \\ &\qquad \text{(direct photoionization in } 4d \text{ subshell)} \\ &\qquad \hookrightarrow Xe^{6+}\,[Kr]\,4d^{10}5s^2 5p^0 + e^- \text{ (Auger decay)}. \end{aligned}$$

All other Xe^{5+} $4d^{-1}$ levels contribute to the intensity of the single ionization cross section above the $4d^{-1}$ thresholds as it is visible in the high energy part of Fig. 6, the $4d^{-1}$ hole

decaying via fluorescence to the ground level of the Xe^{5+} ion. The $4d$ direct photoionization cross section is then obtained from the addition of the single and double ionization cross sections above the $4d^{-1}$ thresholds. The single ionization cross section includes also the contribution of the $5p$ and $5s$ cross sections which can be neglected in first approximation, because the measured single ionization cross section at lower photon energy is already rather small (1.30 ± 0.22 Mb at 65 eV). This addition gives a value of 19 ± 3 Mb for the $4d$ cross section at 120 eV photon energy, close to threshold. This value is only slightly lower than the one measured for the lower members of the Xe isonuclear series, showing that, even for Xe^{4+}, the collapse of the $4f$ wave function is not yet complete, however.

In the experimental spectrum of Fig. 9, the signal appears around 102 eV, and then increases slowly until a clear step at 118.6 eV. If we interpret this step as the double ionization threshold for the Xe^{4+} ions in the ground level (process $Xe^{4+}\,[Kr]\,4d^{10}5s^25p^2\,{}^3P_0 + h\nu \rightarrow Xe^{6+}\,[Kr]\,4d^{10}5s^2\,{}^1S_0 + e^-$), we expect the signal to appear only at photon energies above the double ionization threshold for the ions in the $^1S_0$ metastable level, i.e., 112.3 eV. The signal below this energy can only be produced from Xe^{4+} ions populated in more highly excited metastable levels, such as $Xe^{4+}\,[Kr]\,4d^{10}5s5p^3\,{}^5S_2$. These levels are metastable only if the approximation of the *LS* coupling is valid. Then the small line at 103.4 eV photon energy would be due to a resonant Auger decay process:

$$
\begin{aligned}
&Xe^{4+}\,[Kr]\,4d^{10}5s5p^3 + h\nu \\
&\quad \rightarrow Xe^{4+}\,[Kr]\,4d^9 5s5p^3 np,mf \\
&\qquad (n>4, m>3)\ \text{(photoexcitation)} \\
&\quad \hookrightarrow Xe^{5+}\,[Kr]\,4d^9 5s^2 5p^2 + e^-\ \text{(decay step 1)} \\
&\quad \hookrightarrow Xe^{6+}\,[Kr]\,4d^{10}5s^2 + e^-\ \text{(decay step 2)}.
\end{aligned}
$$

C. Xe^{5+} ion

The experimental determination of the variation of the single photoionization cross sections of Xe^{5+} ion between 60 and 130 eV photon energy is shown in the upper panel of Fig. 10. The ground level of the Xe^{5+} ion is $[Kr]\,4d^{10}5s^25p^1\,{}^2P_{1/2}$. The $J=3/2$ level with the same configuration has a calculated excitation energy of 1.900 eV. It is metastable and contributes also to the observed signal. The results of our MCDF calculations (L form) are displayed in the lower panel of Fig. 10. As previously, it was obtained assuming a statistical population of the two levels in the ion beam, after convolution by a Gaussian profile of FWMH equal to 100 meV representing the experimental band pass. The energy range here extends from the first ionization threshold, calculated to be at 65.565 eV and corresponding to the $Xe^{6+}\,[Kr]\,4d^{10}5s^25p^0\,{}^1S_0$ level (labeled $5p^{-1}$ in Fig. 10) to the $4d^{-1}$ thresholds (calculated between 127.36 and 132.70 eV). A magnification of the region of the $4d \rightarrow 5p$ excitations is shown in Fig. 11. The measured and calculated energies, and the oscillator strengths (both L and V form) of the main resonances are given in Table V, together with a tentative assignment based on our MCDF calculations. Clearly, for the Xe^{5+} ion, the spectrum is completely dominated now by strong $4d \rightarrow mf, np$ excitations. The intensity within the structures 4, 7, 9 looks like in a $4d \rightarrow nf$ Rydberg series, with $n=4$, 5, and 6, respectively. Above the $4d^{-1}$ thresholds, the direct photoionization cross section is strongly reduced. At 130 eV photon energy, the measured cross section is 11.3 ± 2.4 Mb. Nevertheless, weaker resonant ionization processes can still contribute to the signal. When moving to more highly charged ions, it becomes more and more difficult to measure low cross section values because of the decrease of the density of ions in the interaction region. No signal was detected in the double ionization channel ($5p^{-1}5s^{-1}$) above 155.25 eV, i.e., the energy we have calculated for the threshold of this process. Above the $4d^{-1}$ thresholds, the whole intensity of the photoionization cross section in the $4d$ subshell is found in the single ionization channel.

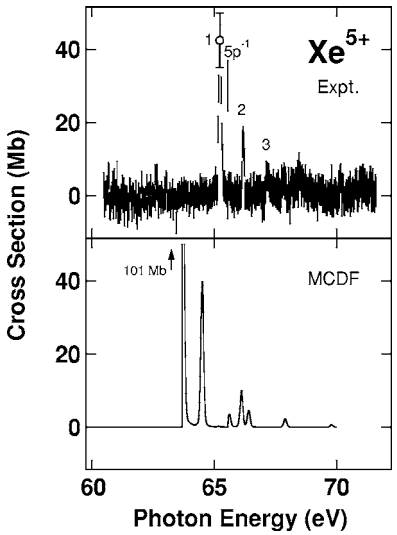

FIG. 11. Variation of the photoionization cross section of the Xe^{5+} ion in the region of the $4d \rightarrow 5p$ excitations. Upper panel: experiment. The excitation band pass is of the order of 120 meV. The open point gives the absolute value of the cross section. The numbers above the resonant structures refer to Table V. Lower panel: results of our MCDF calculations (L form) obtained assuming a statistical population of the ions in the ground and metastable levels.

The measured intensity of the $4d \rightarrow 5p$ transitions, shown in Fig. 11 (lines 1–3), is very low compared to the Xe^{4+} ion. The MCDF calculations, however, predict a total oscillator strength $f=0.78$ in the L form for the sum of all the $4d \rightarrow 5p$ transitions ($f=0.81$ in the V form), i.e., a value that is at least of the same intensity as in the Xe^{4+} case. This results from the fact that the energies of most of these transitions are below the first ionization threshold (labeled $5p^{-1}$ in Fig. 11). Then 90% of the levels with the $Xe^{5+}\,[Kr]\,4d^95s^25p^2$ configuration are decaying via fluorescence to the ground level of Xe^{5+}. According to our calculations, all observed lines are produced from ions in the $^2P_{3/2}$ metastable level. The calculated oscillator strengths of the transitions involved in both lines 1 and 2 using L and V form are in good agreement with the experiment, but the energies are more difficult to compare. A strong line is visible in the

TABLE V. Energies (column 2) and integrated oscillator strengths (column 4) of the $4d \rightarrow 5p$ and $4d \rightarrow np, mf$ ($n>5$, $m>3$) transitions in the Xe^{5+} ion. The numbers in parentheses give the uncertainty on the last figure. The experimental data are compared with the results of our MCDF calculations (energies: column 3; oscillator strengths calculated in the *L* and *V* form assuming a statistical population of the levels in the ion beam: columns 5 and 6, respectively). A tentative assignment of the lines is presented using the MCDF calculations (column 7).

	Energy (eV)		Oscillator strength	MCDF		
Line	Expt.	MCDF	Experiment	*L*	*V*	Assignment
1	65.26 (2)	64.518	0.059 (12)	0.055	0.057	$^2P_{3/2} \rightarrow 5p\ ^2D_{3/2}$
2	66.21 (4)	67.910	0.014 (3)	0.013	0.014	$^2P_{3/2} \rightarrow 5p\ ^2D_{5/2}$
3	67.27 (8)		0.009 (2)			
4	94.48 (3)	95.923, 96.060	3.04 (55)	4.202	2.802	$^2P_{3/2} \rightarrow 4f\ ^2P_{3/2}, ^2D_{5/2}$
		95.649, 96.007				$^2P_{1/2} \rightarrow 4f\ ^2D_{3/2}, ^2P_{1/2}$
5	95.7–101.0		0.86 (15)	0.318	0.243	$6p$
6	101–107		0.57 (10)	0.227	0.142	$5f$
7	108.35 (3)	108.751, 108.775	2.05 (37)	2.122	1.321	$^2P_{3/2} \rightarrow 5f\ ^2P_{1/2}, ^2D_{5/2}$
		108.440, 108.636				$^2P_{1/2} \rightarrow 6f\ ^2P_{1/2}, ^2D_{3/2}$
8	112–114.6		0.34 (6)	0.491	0.293	$5f, 6f$
9	116.23 (3)		0.67 (12)	0.782	0.466	$6f$
10	119.21 (10)		0.40 (7)	0.831	0.488	$7f$
11	121.60 (5)		0.32 (6)	0.624	0.353	$^2P_{1/2} \rightarrow 8f, ^2P_{3/2} \rightarrow 7f$

theoretical spectrum at 63.7 eV. It is also predicted to be produced by ions in the $^2P_{3/2}$ metastable level. It is sitting right at the ionization threshold for these ions. Its absence in the experimental spectrum is probably due to a calculated threshold energy value that is too high, allowing this line to artificially decay via autoionization.

The agreement between the *L* and *V* form is far from being as good in the energy region of the $4d \rightarrow mf, np$ excitations. When compared to the experiment, the average of the two form values reproduces quite well the $4d \rightarrow nf$ series, but the calculated energy is too high by 1.5 eV for the $4d \rightarrow 4f$ structure (number 4 in Fig. 10). Clearly, there is also a broadening of the resonance which is not included in the calculations. It results from the short life time of the Xe^{5+} [Kr] $4d^9 5s^2 4f 5p$ excited configuration which probably decays with a very high rate to the ground level of Xe^{6+}, mainly via $4f \rightarrow 4d$ recombination. Considering only the dominant configuration in the final state, our calculations attribute 60% of the intensity of the structure 4 to $4d \rightarrow 4f$ transitions, and 40% to $4d \rightarrow 6p$ transitions. The remaining of the $4d \rightarrow 6p$ transitions is observed on the high-energy side (structure 5) of the $4d \rightarrow 4f$ structure. In the same way, structure 7 is composed of unresolved $4d \rightarrow 5f$ (for 42%), $4d \rightarrow 7p$ (33%), and $4d \rightarrow 6f$ (25%) transitions. The intensity of the broom resonance, observed around 126 eV in the theoretical spectrum, is now strongly reduced.

D. Xe^{6+} ion

The variation of the photoionization cross sections measured at Super ACO and ASTRID is shown in the upper and middle panels of Fig. 12, respectively. They are compared to the results of the MCDF calculations obtained in the *L* form, and after convolution with a Gaussian profile of 0.8 eV FWMH. The ground level of the Xe^{6+} ion is

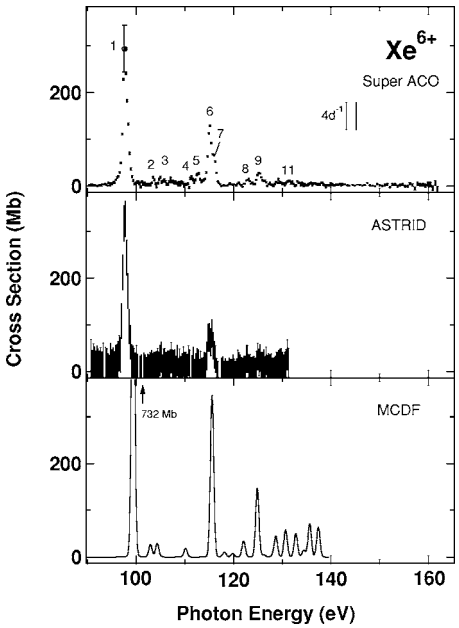

FIG. 12. Variation of the single photoionization cross sections of the Xe^{6+} ion as a function of the photon energy (from the detection of the Xe^{7+} ions). Upper panel: measurements at Super ACO with an averaged band pass of 0.8 eV; middle panel: measurements at ASTRID (averaged band pass of 1 eV); lower panel: results of our MCDF calculations (*L* form). The numbers on the lines refer to Table VI.

TABLE VI. Energies (column 2) and integrated oscillator strengths (measured at Super ACO, column 4, and at ASTRID, column 5) of the resonant lines for the Xe^{6+} ion. The numbers in parentheses give the uncertainty on the last figure. The experimental data are compared to the results of our MCDF calculations (energies: column 3; oscillator strengths calculated in the *L* (column 6) and *V* form (column 7) assuming a statistical population of the levels in the ion beam). The last column gives the final level of the transition according to our calculations.

			Oscillator strength				
	Energy (eV)		Experiments		MCDF		Assignment
Line	Expt.	MCDF	SACO	ASTRID	*L*	*V*	(final state)
1	97.70 (3)	99.347	3.63 (66)	3.75 (81)	5.782	3.774	$4f\ ^1P_1$
2	103.52 (7)	102.910	0.06 (2)		0.209	0.170	$6p\ ^3P_1$
3	105.22 (15)	104.285	0.13 (4)		0.227	0.184	$6p\ ^3P_1$
4	111.32 (7)	110.123	0.08 (2)		0.143	0.084	$5f\ ^3D_1$
5	112.68 (8)		0.24 (5)				
6	115.10 (3)	115.570	1.05 (19)	1.08 (16)	2.729	1.605	$5f\ ^1P_1$
7	116.04 (6)		0.38 (8)				
8	122.98 (12)	122.050	0.09 (3)		0.273	0.150	$6f\ ^3D_1$
9	125.27 (7)	124.859	0.26 (5)		1.155	0.631	$6f\ ^1P_1$
10	129.23 (15)	128.676	0.06 (2)		0.354	0.185	$7f\ ^3D_1$
11	131.34 (18)	130.659	0.06 (3)		0.436	0.226	$7f\ ^1P_1$

$[Kr]\ 4d^{10}5s^2\ ^1S_0$. The measured and calculated energies and oscillator strengths of the lines are reported in Table VI. Because of the low current of ions available in the experiment, only the two most intense lines (1 and 6) are visible in the ASTRID spectrum. Nevertheless, the integrated oscillator strength for these lines is in very good agreement with the ones independently determined at Super ACO. According to our calculations, the first ionization threshold for the Xe^{6+} ion ($5s^{-1}$) is at 89.56 eV, i.e., above the energy of the $4d \rightarrow 5p$ transitions (we have calculated it to be around 67 eV, and it has been observed at 67.23 eV by Blackburn *et al.* [11]). As a consequence, the Xe^{6+} excited levels populated by these transitions decay via fluorescence only, and cannot be observed in these experiments. We have calculated the opening of the double ionization channel ($5s^{-2}$) to be at 193.83 eV. It is outside of the photon energy range of the beam lines used in our work. The cross section to this channel is expected to be very small close to threshold, since only direct double photoionization can contribute to the spectrum until the energy region of the $4p$ excitations is reached (we have calculated the $4p^{-1}$ thresholds to be around 240 eV).

Despite a simplification due to the smaller number of levels in the initial state, the Super ACO spectrum is quite similar to the one recorded for the Xe^{5+} ion. It is dominated by $4d \rightarrow nf$ Rydberg series converging to the $4d^{-1}$ thresholds, which are calculated at 143.16 and 145.15 eV. The intensity of the $4d \rightarrow 4f$ transitions (line 1) is still increased as compared to Xe^{5+}. The MCDF calculations show the best results when using the *V* form to calculate the intensity of this line, while the *L* form always provides higher values. The predicted energies are 1.6 eV higher than the experimental values. From a fitting procedure of the experimental spectrum with a Voigt profile, we determined a natural width of 0.5 ± 0.1 eV, which gives more evidence for the strong $4d$ and $4f$ wave-function overlap. Taking into account this width in the MCDF spectrum brings the cross section at the top of line 1 into better agreement with the experimental value. For the second most intense structure (line 6), corresponding mainly to $4d \rightarrow 5f$ transitions, the shoulder on the high-energy side (line 7 at 116.04 eV) is not reproduced by the calculations. Blackburn *et al.* [11] have observed a line at 116.01 eV and have identified it as corresponding to the transition $4d \rightarrow 5f\ ^1P$. Nevertheless, they assign a line at 109.32 eV, not observed in our spectrum, to the $4d \rightarrow 5f\ ^3P$ transition. Another explanation for line 7 might be the presence of Xe^{6+} ions produced in metastable states in the ECRIS, e.g., the Xe^{6+} $[Kr]\ 4d^{10}5s5p\ ^3P_0$ level. We have calculated its excitation energy to be about 12 eV. According to our calculations, the Xe^{6+} $[Kr]\ 4d^{10}5s4f$ configuration also gives four metastable levels around 35 eV excitation energy. The energies of the $4d \rightarrow 4f$ and $4d \rightarrow 5f$ transitions from these metastable levels are calculated to be around 92 and 109 eV, respectively. Their oscillator strengths are predicted to be one order of magnitude higher than the oscillator strengths of the same transitions for the ions in the ground state. Such intense structures are not observed in the experimental spectrum. This indicates that the calculated excitation energy from the Xe^{6+} $[Kr]\ 4d^{10}5s4f$ configuration is mistakenly placed below the energy of the Xe^{6+} $[Kr]\ 4d^{10}5s5d$ configuration, showing that the $[Kr]\ 4d^{10}5s4f$ configuration is not metastable. The broom resonance has disappeared in the theoretical cross section.

Between 145 and 150 eV photon energy, the average of the measured direct photoionization cross section values is 2.0 ± 0.4 Mb, which is significantly smaller than in the case of the Xe^{5+} ion. This cross section includes the contribution of the direct photoionization processes in both the $5s$ and $4d$ subshells.

TABLE VII. Experimental values of the integrated oscillator strengths for the $4d$ subshell for neutral xenon and Xe^{n+} ions up to $n=6$. Columns 2 and 3 show the total oscillator strengths of all $4d \rightarrow 5p$ and the $4d \rightarrow 4f$ transitions, respectively. Columns 4 and 5 give the partition of the oscillator strengths of the $4d \rightarrow nl, \varepsilon l$ transitions into their various components. The total oscillator strengths of the $4d$ subshell are shown in column 6. The data for Xe, Xe^+, and Xe^{2+} are from Refs. [5,18].

Target	$4d \rightarrow 5p$	$4d \rightarrow 4f$	$4d \rightarrow mf,np$ $m>3,\ n>4$	$4d \rightarrow \varepsilon f, \varepsilon p$	Total
Xe	0		0	10.7	10.7
Xe^+	0.2		~0	9.4	9.6±1.0
Xe^{2+}	0.6		0.8	8.7	9.5±1.0
Xe^{3+}	0.43±0.12	1.5±0.2	4.5±0.6	5.2±0.8	9.7±1.4
Xe^{4+}	0.82±0.14	2.9±0.6	8.7±1.5	3.5±0.7	12.1±2.4
Xe^{5+}	0.13±0.2	3.0±0.6	10.4±2.1	~0	10.5±1.9
Xe^{6+}		3.7±0.5	7.7±1.5	0.28±0.06	8.0±1.6

E. Xe isonuclear series

Table VII summarizes the measured oscillator strengths for the $4d$ electrons in the ions of the Xe isonuclear sequence. Results on Xe, Xe^+, and Xe^{2+} are from Refs. [5,18]. Results for Xe^{3+} to Xe^{6+} ions are from the present work. The table given in Ref. [19] is similar, but is limited to Xe ions up to Xe^{3+}. It gives a value for the total oscillator strength for Xe^{3+}, $f=10.5\pm2.6$, in good agreement with our value, but a higher oscillator strength is attributed to the discrete $4d \rightarrow nl$ transitions ($f=5.88\pm1.47$). This is due to the use of different integration limits for the determination of the oscillator strengths. As explained before, we have assumed that, above the first $4d^{-1}$ ionization threshold (around 95 eV for the ions in the $Xe^{3+}\ ^2P_{3/2}$ metastable level), most of the intensity of the double ionization cross section is due to the direct photoionization process in the $4d$ subshell. Only the part of the cross section below 95 eV was attributed to the $4d \rightarrow nl$ transitions via resonant Auger decay processes. Consequently, we kept the same 95-eV limit between discrete and continuum transitions for the single photoionization cross section, while the authors of Ref. [19] estimated this limit to be at 104 eV. This example illustrates the difficulty to give an accurate partition of the total oscillator strength in the case of Xe^+ to Xe^{4+} ions, especially when the $4d^{-1}$ thresholds are extending over a broad energy range due to momentum coupling and/or to the presence of several levels populated in the ion beam. The upper limit we have used is 160 eV for all charge states.

The partition of the oscillator strength between the $4d \rightarrow np, mf$ $(n>4, m>3)$ discrete excitations and the $4d \rightarrow \varepsilon p, \varepsilon f$ continuum transitions gives an indication of the degree of collapse of the $4f$ wave function in the inner well. The more the $4f$ wave function is collapsed, the higher the oscillator strength must be in the discrete part of the spectrum. This partition is given in Table VII, which shows the oscillator strength for the sum of the $4d \rightarrow 5p$ and $4d \rightarrow 4f$ transitions. The oscillator strength of the $4d \rightarrow 4f$ discrete transitions is close to zero in neutral Xe, and continuously increases up to the Xe^{4+} ion. The intensity of the higher $4d \rightarrow nl$ transitions is still increasing up to Xe^{5+}. Simultaneously, the intensity of the $4d \rightarrow \varepsilon p, \varepsilon f$ continuum transitions is continuously decreasing up to Xe^{5+} ion, demonstrating that the collapse of the $4f$ wave function is only complete for this ion.

TABLE VIII. Calculated oscillator strengths (averaged values of the L and V form) for the discrete $4d \rightarrow nl$ transitions for the ions along the isonuclear series of Xe. The labeling of each column is the same as in Table VII. In the column 5 is given the oscillator strength for the broom resonance. The $4d \rightarrow \varepsilon l$ oscillator strength has not been calculated.

Target	$4d \rightarrow 5p$	$4d \rightarrow 4f$	$4d \rightarrow mf,np$ $m>3,\ n>4$	Broom resonance	Total
Xe^{3+}	0.435	0.900	3.03	7.10	10.13
Xe^{4+}	0.603	2.300	6.09	4.81	10.90
Xe^{5+}	0.795	3.500	8.78	2.56	11.34
Xe^{6+}	0.989	4.778	10.81	0.79	11.60

This transfer of the oscillator strength from the discrete to the continuum part of the spectrum is a consequence of the partial sum rule formulated by Kronig and Kramers [37]. They predicted that the total oscillator strength for the excitation ionization of the electrons of a given subshell can be approximated by the number of electrons in the subshell. It constitutes an extension of the Thomas-Reiche-Kuhn sum rule which is only exact for the total number of electrons in the atom. Kjeldsen *et al.* [5] have shown that the measured total oscillator strength for $4d$ electron excitations was always compatible with the value of 10 (the number of electrons in the $4d$ subshell) for the ions of the isonuclear series of I, Xe, and Ba, as well as of the isoelectronic series of Xe, for ions with charge state between −1 and 2. The present work extends the validity of the partial sum rule up to the Xe^{5+} ion. It is likely that this rule is even valid for the Xe^{6+} ion, since the $f=8.0\pm1.6$ value we measured for the total oscillator strength, as it is shown in Table VII for this ion, does not include the contribution of the $4d \rightarrow 5p$ transitions. This contribution should be equal to 1 according to our MCDF calculations.

The oscillator strengths obtained from the MCDF calculations are given in Table VIII for Xe^{3+} to Xe^{6+} ions. They are the average of the values obtained in the L and V form. The general increase of the intensity of the discrete $4d \rightarrow nl$ transitions is qualitatively well described along the isonuclear sequence, but the oscillator strengths are systematically lower than the measured values. For all charge states of the Xe ions, our MCDF calculations show the existence of some lines with very large oscillator strengths at high photon energy. These lines are very close and tend to overlap to form an unresolved structure we have called broom resonance. Their oscillator strength is given in the column 5 of Table VIII. It is particularly strong for the lowest charge states of the Xe ion. The maximum amplitude of the broom resonance decreases by a factor of about 1.5 between Xe^{3+} and Xe^{4+}. For Xe^{5+}, the maximum amplitude of the broom resonance is drastically reduced and this structure has almost

disappeared for Xe^{6+}. The energy position and the intensity of these structures appear to be extremely sensitive to the choice of the excited configurations, mainly the $4d^9 5s^2 5p^m nf$ configurations where $m=2(3)$ for $Xe^{4+}(Xe^{3+})$ and $n=4-9$, respectively. For example, when the $4d^{10}5s^2 5p^3$ and the $4d^9 5s^2 5p^3 4f$ configurations are only considered in the case of the Xe^{3+} ion, the broom resonance is localized at about 98 eV. It is shifted to higher energies when the other excited configurations are successively introduced in the calculations and tends to converge to an energy close to the $4d^{-1}$ thresholds. For Xe^{3+}, the autoionization rates of the upper levels involved in the broom resonance have been calculated using the Fermi gold rule. The final states resulting from the excitation of the $4d^{10}5s^2 5p^2$ and $4d^{10}5s^1 5p^3$ configurations have been considered. Values close to 1.5×10^{15} s^{-1} have been obtained. They are too small to explain why the broom resonance is not experimentally observed, giving another evidence that these structures have no physical significance. We can suspect that a strong coupling occurs between bound-bound and bound-free channels in the vicinity of the $4d^{-1}$ thresholds. The total oscillator strength (last column in Table VIII), including the contribution of the broom resonance, is always calculated being close to 10, although bound-free channels are not included in the calculations. Then the oscillator strength of the broom resonance could be partially or totally transferred and diluted in the direct photoionization cross sections. In the case of a partial transfer, the remaining oscillator strength should be redistributed in the overall $4d$-nf transition spectrum. The broom resonance could be also interpreted as the signature of the incomplete $4f$ orbital collapse in Xe^{3+} and Xe^{4+}.

V. SUMMARY AND CONCLUSION

Absolute photoionization cross sections of Xe^{3+} to Xe^{6+} ions have been measured over an extended photon energy range, from the first ionization threshold up to 160 eV. Cross sections for single and double ionization have been obtained. In the case of Xe^{3+} and Xe^{6+} ions, two completely independent setups, both based on the merged beams technique, have been used. MCDF calculations were performed to interpret the spectra in the region of $4d$ electron excitations. Our results confirm that such studies along isonuclear and isoelectronic sequences are powerful tools to follow gradual changes in electron correlation effects occurring when outer electrons are successively removed or when the charge of the nucleus is increasing. The partition of the oscillator strength between the discrete photoexcitation and the direct photoionization channels in the $4d$ subshell did allow us to follow accurately the gradual collapse of the $4f$ wave function in these ions of the isonuclear series of Xe.

The main difficulty in the interpretation of the experimental results, especially when ECRIS is used for the production of the ionic target, is the determination of the relative population of all metastable levels present in the ion beam. A completely experimental determination of the metastable contribution is not possible most of the time. In some cases the populations can be estimated using theoretical data, like the oscillator strength of a well resolved resonance or the intensity of a direct photoionization cross section close to threshold. Nevertheless, in heavy ions like Xe^{n+}, such a procedure cannot apply. The use of a high-resolution beam line, similar to the one available at the ALS or, in the near future, at the next French synchrotron radiation facility SOLEIL, would certainly be of great assistance for the estimation of such populations. In parallel, more theoretical investigations are needed, in particular to further elucidate the mechanism responsible for the broom resonance in the calculations.

ACKNOWLEDGMENTS

We would like to acknowledge the support of the Laboratoire pour l'Utilisation du Rayonnement Electromagnétique (LURE), funded by the Centre National de la Recherche Scientifique (CNRS), of the Commissariat à l'Energie Atomique (CEA DAM), and of the European Community-Access to Research Infrastructure Action of the Improving Human Potential Programme. We are grateful to the staffs of the LURE at the University of Orsay and of the Institute for Storage Ring Facilities (ISA) at the University of Aarhus for their assistance throughout the duration of the project.

[1] D. L. Ederer, Phys. Rev. Lett. **13**, 760 (1964).
[2] J. W. Cooper, Phys. Rev. Lett. **13**, 762 (1964).
[3] M. Ya. Amusia, J. Phys. B **23**, 393 (1990).
[4] T. B. Lucatorto, T. J. McIlrath, J. Sugar, and S. M. Younger, Phys. Rev. Lett. **47**, 1124 (1981).
[5] H. Kjeldsen, P. Andersen, F. Folkmann, J. E. Hansen, M. Kitajima, and T. Andersen, J. Phys. B **35**, 2845 (2002).
[6] C. W. Clark, J. Opt. Soc. Am. B **1**, 626 (1984).
[7] J. M. Bizau, J. M. Esteva, D. Cubaynes, F. J. Wuilleumier, C. Blancard, A. C. La Fontaine, C. Couillaud, J. Lachkar, R. Marmoret, C. Rémond, J. Bruneau, D. Hitz, P. Ludwig, and M. Delaunay, Phys. Rev. Lett. **84**, 435 (2000).
[8] I. C. Lyon, B. Peart, J. B. West, and K. Dolder, J. Phys. B **19**, 4137 (1986).
[9] T. Koizumi, Y. Awaya, A. Fujino, Y. Itoh, M. Kitajima, Y. M. Kojima, M. Oura, R. Okuma, M. Sano, T. Seikioka, N. Watanabe, and F. Koike, Phys. Scr., T **T73**, 131 (1997).
[10] M. Sano, Y. Itoh, T. M. Koizumi, S. D. Kravis, M. Oura, T. Sekioka, N. Watanabe, Y. Awaya, and F. Koike, J. Phys. B **29**, 5305 (1996).
[11] J. Blackburn, P. K. Carroll, J. Costello, and G. O'Sullivan, J. Opt. Soc. Am. **73**, 1325 (1983).
[12] R. M. D'Arcy, J. T. Costello, E. T. Kennedy, J. P. Mosnier, C. McGuinness, and G. O'Sullivan, J. Phys. B **33**, 1383 (2000).
[13] G. O'Sullivan, C. McGuinness, J. T. Costello, E. T. Kennedy, and B. Weinmann, Phys. Rev. A **53**, 3211 (1996).
[14] W. Svendsen and G. O'Sullivan, Phys. Rev. A **50**, 3710 (1994).

[15] U. Köble, L. Kiernan, J. T. Costello, J. P. Mosnier, E. T. Kennedy, V. K. Ivanov, V. A. Kupchenko, and M. S. Shendrik, Phys. Rev. Lett. **74**, 2188 (1995).
[16] H. Kjeldsen, P. Andersen, F. Folkmann, H. Knudsen, B. Kristensen, J. B. West, and T. Andersen, Phys. Rev. A **62**, 020702(R) (2000).
[17] Y. Itoh, A. Ito, M. Kitajima, T. Koizumi, T. M. Kojima, H. Sakai, M. Sano, and N. Watanabe, J. Phys. B **34**, 3493 (2001).
[18] P. Andersen, T. Andersen, F. Folkmann, V. K. Ivanov V, H. Kjeldsen, and J. B. West, J. Phys. B **34**, 2009 (2001).
[19] E. D. Emmons, A. Aguilar, M. F. Gharaibeh, S. W. J. Scully, R. A. Phaneuf, A. L. D. Kilcoyne, A. S. Schlachter, I. Alvarez, C. Cisneros, and G. Hinojosa, Phys. Rev. A **71**, 042704 (2005).
[20] J. M. Bizau, D. Cubaynes, J. M. Esteva, F. J. Wuilleumier, C. Blancard, J. Bruneau, J. P. Champeaux, A. Compant La Fontaine, C. Couillaud, R. Marmoret, C. Rémond, D. Hitz, M. Delaunay, N. Haque, P. C. Deshmukh, H. L. Zhou, and S. T. Manson, Phys. Rev. Lett. **87**, 273002 (2001).
[21] J. P. Champeaux, J. M. Bizau, D. Cubaynes, C. Blancard, S. Nahar, D. Hitz, J. Bruneau, and F. J. Wuilleumier, Astrophys. J., Suppl. Ser. **148**, 583 (2003).
[22] J. M. Bizau, E. Bouisset, C. Blancard, J. P. Champeaux, A. Compant La Fontaine, C. Couillaud, D. Cubaynes, D. Hitz, C. Vinsot, and F. J. Wuilleumier, Nucl. Instrum. Methods Phys. Res. B **205**, 290 (2003).
[23] H. A. Bethe and E. E. Salpeter, in *Handbuch der Physik* (Springer-Verlag, Berlin, 1957), Vol. 35, p. 390.
[24] H. Kjeldsen, F. Folkmann, J. van Elp, H. Knudsen, J. B. West, and T. Andersen, Nucl. Instrum. Methods Phys. Res. B **234**, 349 (2005).
[25] J. A. R. Samson, *Techniques of Vacuum Ultra Violet Spectroscopy* (John Wiley & Sons, New York, 1967), p. 266.
[26] J. Bruneau, J. Phys. B **17**, 3009 (1984).
[27] S. J. Rose, N. C. Pyper, and I. P. Grant, J. Phys. B **11**, 755 (1978).
[28] J. C. Slater, *Quantum Theory of Molecules and Solids* (McGraw-Hill, New York, 1974), Vol. 4.
[29] U. Fano and J. W. Cooper, Rev. Mod. Phys. **40**, 441 (1968).
[30] A. Fahlman, M. O. Krause, T. A. Carlson, and A. Svensson, Phys. Rev. A **30**, 812 (1984).
[31] J. G. Reyna Almandos, F. Bredice, M. Gallardo, C. J. B. Pagan, H. O. Di Rocco, and A. G. Trigueiros, Phys. Rev. A **43**, 6098 (1991).
[32] A. J. J. Raassen, Y. N. Joshi, and J. F. Wyart, Phys. Lett. A **154**, 453 (1991).
[33] J. E. Hansen, Phys. Scr. **21**, 510 (1980).
[34] H. Smid and J. E. Hansen, J. Phys. B **14**, L811 (1981).
[35] C. McGuinness, Ph.D. thesis, National University of Ireland, Galway, 1996.
[36] J. B. West and J. Morton, At. Data Nucl. Data Tables **22**, 103 (1978).
[37] R. Kronig and H. A. Kramers, Z. Phys. **48**, 147 (1928).